Digest Journal of Nanomaterials and Biostructures

Dig. J. Nanomater. Bios. **2026**; 21(3): 58019
https://doi.org/10.31083/DJNB58019

Original Research

Optoelectronic, Photo-Catalytic and Thermodynamic Properties of Ba-Based Spinels ($BaLu_2X_4$, X = S, Se) for Energy Harvesting Applications Explored Using First-Principles Calculations

Saba Maqsood[1,*], Hosam O. Elansary[2], Muhammad Aamir Javed[3], Sohail Mumtaz[4], Hafiz Hamid Raza[5], Muhammad Usman Khan[6]

[1]Department of Physics, Govt Graduate College of Science, 54000 Lahore, Pakistan
[2]Prince Sultan Bin Abdulaziz International Prize for Water Chair, Prince Sultan Institute for Environmental, Water and Desert Research, King Saud University, 11451 Riyadh, Saudi Arabia
[3]Department of Mathematics, GC University, 54000 Lahore, Pakistan
[4]Department of Electrical and Biological Physics, Kwangwoon University, 01897 Seoul, Republic of Korea
[5]Centre for Advanced Studies in Physics (CASP), GC University, 54000 Lahore, Pakistan
[6]National Key Laboratory of Tunable Laser Technology, Institute of Optoelectronics, Department of Electronics Science and Technology, Harbin Institute of Technology, 150080 Harbin, Heilongjiang, China
*Correspondence: saba.maq.55@gmail.com (Saba Maqsood)
Academic Editor: Carmen-Georgeta Ristoscu
Submitted: 30 December 2025 Revised: 24 March 2026 Accepted: 30 March 2026 Published: 14 September 2026

Abstract

Background: Chalcogenide spinels are promising semiconducting materials for optoelectronic, photocatalytic, and renewable energy applications because of their structural stability and tunable electronic properties. This study systematically investigates the structural, electronic, optical, elastic, thermodynamic, and photocatalytic characteristics of $BaLu_2S_4$ and $BaLu_2Se_4$ using first-principles calculations. **Methods:** Density functional theory calculations were performed using the full-potential linearized augmented plane wave method within the Perdew-Burke-Ernzerhof generalized gradient approximation (PBEsol-GGA) framework. The Tran–Blaha modified Becke–Johnson potential was employed for accurate electronic and optical properties, while thermodynamic behavior was evaluated using the quasi-harmonic Debye model. **Results:** Both compounds exhibited negative formation energies and satisfied the Born stability criteria, thus being thermodynamically and mechanically stable. The indirect band gaps of $BaLu_2S_4$ and $BaLu_2Se_4$ were obtained as 3.1 and 2.8 eV, respectively. Selenium substitution expanded the lattice, decreased the band gap, enhanced visible-light absorption, and improved photocatalytic performance. $BaLu_2S_4$ exhibited a higher mechanical rigidity and thermal stability, whereas $BaLu_2Se_4$ showed greater anharmonicity, thermal expansion, and hydrogen evolution capability owing to its favorable band-edge alignment. **Conclusions:** $BaLu_2S_4$ and $BaLu_2Se_4$ are stable semiconducting spinels with excellent optoelectronic and thermodynamic properties. $BaLu_2Se_4$ is the more favorable candidate for visible-light-driven photocatalytic hydrogen production based on its more negative CBM and stronger reduction potential.

Keywords: spinels; first-principles calculations; optoelectronic properties; transport properties; elastic properties; thermodynamic properties

1. Introduction

The growing demand for clean and sustainable energy technologies has intensified the search for semiconducting materials capable of efficient light absorption and energy conversion [1,2,3]. Materials with suitable band gaps, strong optical absorption, and stable crystal structures are particularly important for applications such as optoelectronics, photovoltaics, and photocatalytic water splitting [4,5]. In this context, chalcogenide-based semiconductors have attracted considerable attention due to their tunable electronic structures, high absorption coefficients, and favourable charge transport properties [6]. Among the various classes of chalcogenides, spinel-type compounds with the general formula AB_2X_4 (A and B = metal cations; X = S, Se, or Te) offer a versatile structural platform for tailoring electronic and optical properties through compositional substitution [7,8]. The cubic spinel framework allows flexible cation distribution between tetrahedral and octahedral sites, which strongly influences band dispersion and optical response. Recent investigations have shown that chalcogenide spinels exhibit a broad range of band gaps depending on their chemical composition. For example, $ZnSc_2Se_4$ and $CdSc_2Se_4$ have been reported to possess direct band gaps in the range of ~0.9–1.2 eV, making them suitable for infrared and visible applications [9,10]. Similarly, $MnIn_2S_4$ and $MgIn_2S_4$ spinels exhibit band gaps between 2.0 and 2.4 eV, enabling visible-light-driven photocatalytic activity [11]. Other ternary chalcogenide spinels such as $CuCo_2S_4$ and $FeIn_2S_4$ have shown band gaps near 1.5–2.2 eV with promising optoelectronic and electrochem-

ical properties [12]. These examples demonstrate the strong dependence of the band gap on the nature of both cations and chalcogen atoms, highlighting the importance of compositional engineering.

In photocatalytic applications, not only the magnitude of the band gap but also the relative positions of the conduction band minimum (CBM) and valence band maximum (VBM) with respect to water redox potentials determine hydrogen evolution efficiency [13,14]. Materials with properly aligned band edges and direct electronic transitions are particularly advantageous, as direct band gap semiconductors enable stronger photon absorption and efficient charge carrier generation without phonon assistance. Consequently, systematic theoretical studies are essential to understand how elemental substitution modifies electronic structure and optical response in spinel chalcogenides. In recent years, semiconductor materials have emerged as particularly attractive candidates owing to their adjustable electronic properties, long-term chemical stability, and broad applicability in optoelectronic and photocatalytic technologies [15,16]. In this regard, barium-based lutetium chalcogenide spinels provide a compelling platform for investigating energy-related functionalities, arising from the synergistic incorporation of heavy alkaline-earth and rare-earth elements within a stable structural framework. Among the relatively unexplored members of this class, $BaLu_2S_4$ and $BaLu_2Se_4$ stand out as promising candidates for renewable energy applications. The substitution between sulfur and selenium anions offers a controllable pathway to modify the electronic band structure and optical absorption profile, which is essential for optimizing light–matter interactions.

From an application-oriented perspective, photocatalytic water splitting has emerged as a viable route for sustainable hydrogen production, where the relative positioning of semiconductor band edges with respect to water redox potentials is a decisive factor. Only materials with appropriately aligned conduction and valence bands can simultaneously facilitate hydrogen and oxygen evolution reactions under solar illumination. Chalcogenide spinels are particularly attractive in this context due to their tunable band structures and strong absorption in the visible region. While several magnesium-based spinel compounds have already been investigated for applications in battery systems, thermal technologies, and optical devices, the intrinsic electronic and optical properties of $BaLu_2X_4$ (X = S, Se) remain largely unaddressed, underscoring the importance of their detailed investigation.

Despite growing interest in chalcogenide spinels, Ba-based rare-earth spinels remain relatively unexplored compared to transition-metal analogues. In particular, $BaLu_2X_4$ (X = S, Se) has received limited theoretical attention, even though the presence of heavy alkaline-earth and rare-earth elements may significantly influence lattice stability, orbital hybridization, and optical behavior. Furthermore, substitution of sulfur by selenium is expected to modify lattice parameters and electronic dispersion due to differences in atomic radius and electronegativity, potentially narrowing the band gap and shifting absorption toward the visible region. In this work, we present a systematic first-principles investigation of $BaLu_2S_4$ and $BaLu_2Se_4$ to evaluate their structural, electronic, optical, mechanical, thermodynamic, and photocatalytic properties. Special emphasis is placed on understanding the effect of chalcogen substitution on band structure and optical absorption, as well as comparing the calculated band gaps with previously reported values of related chalcogenide spinels. The findings provide insight into the tunability of Ba-based spinels and their potential suitability for optoelectronic and solar energy applications.

2. Computational Details

For this work, the Full Potential Linearized Augmented Plane Wave Method (FP-LAPW) technique using the WIEN2k code [17] has been used to evaluate the required parameters within the context of density functional theory (DFT). This technique has been applied to both the core state and valence semi-relativistic state. For the evaluation of the ground state properties and to study its behavior concerning structure, the Perdew-Burke-Ernzerhof generalized gradient approximation (PBEsol-GGA) functional [18] was utilized. For this, the calculation of minimum total energy was investigated for different volumes for studied spinels $BaLu_2X_4$ (X = S, Se) compounds. The calculated values came out to be in a close approximation to those observed in experimental studies. Additionally, for $BaLu_2X_4$ (X = S, Se), optoelectronic and thermo-physical properties have also been calculated using the Tran-Blaha modified Becke-Johnson exchange potential (TB-mBJ) potential [19]. These calculations have resulted in an enhanced sequence of attributes in the materials mentioned.

For better convergence, the muffin-tin radius (R_{MT}) with the absolute highest value of the wave vector associated with the reciprocal lattice (K_{max}) is multiplied by eight. Nevertheless, the Fourier potential was employed in the wider interstitial domain with a G_{max} value of 16 Ry. To achieve complete power convergence, which refers to the difference in energy between successive iterations is specified as 0.00001 Ry. An energy cutoff of –6.0 Ry is utilized, and an elastic convergence value of 10^{-3} eV/Å is set. The main and crucial aspect of technique is the choice of k-values, which is determined by determining the optimal number of k-point pairings for conversion of energy. To achieve optimal energy convergence, a total of ~2000 k-points are chosen. This number is determined based on the observation that energy optimizations reach a plateau after this point. Thermodynamic parameters, including free energy, entropy, and specific heat, were derived from total-energy data employing the quasi-harmonic Debye model. Photocatalytic activity was examined by aligning the calculated conduction and valence band edges with respect to

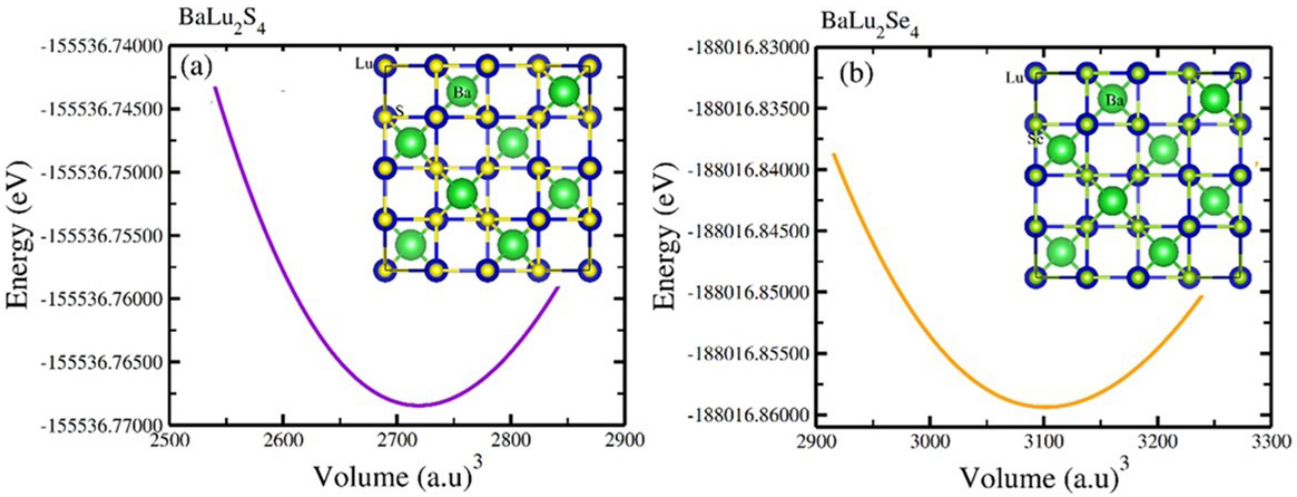

Fig. 1. Volume optimization along their unit cell of spinels (a) $BaLu_2S_4$ and (b) $BaLu_2Se_4$.

the vacuum level and comparing them with standard water redox potentials, enabling assessment of hydrogen and oxygen evolution feasibility.

3. Results and Discussion

3.1 Structural, Optoelectronic and Elastic Properties

3.1.1 Structural Properties

We conducted a structural study to optimize the cubic spinel-like framework of $BaLu_2X_4$ (X = S, Se) and determined the lattice parameter (a_o) and the bulk modulus (B_0). Spinels having ordered cubic crystal structure with space group Fd-3m#227 and their ground state determine by minimum total energy per unit cell. In studied spinels $BaLu_2X_4$, where X represents either S or Se, exhibits a cubic arrangement as depicted in Fig. 1. In the cubic configurations of the examined spinels, the Wyckoff sites of Ba, Lu, and X are selected as follows: Ba is located at each corner of a cube, Lu is positioned at the center of that octahedron, as well as X anion are situated at the center. From the volume optimization, ground state lattice constant (a_o) are calculated and listed in Table 1. Referring to Table 1, we observe that the acquired values for a_o using PBEsol-GGA are comparable to similar spinels $MgLu_2X_4$ (X = S, Se) [20]. According to the data in Table 1, a_o increases from 11.72 to 12.25 Å when S is replaced with Se. This expansion is attributed to the greater atomic radius of Se atom as compared to S atom. Table 1 also show the bulk modulus (B_0) decreases as S atom is replaced by Se in the crystal lattice of spinels $BaLu_2X_4$ (X = S, Se) indicating that the resistance of the crystal lattice to the external compressions decreases. Therefore, the interatomic bonding becomes relatively weaker, reducing the stiffness of the crystal structure. So, the Se-based compound exhibits greater compressibility than the corresponding S-based compound, as reflected by its lower bulk modulus value.

Table 1. The computed lattice parameter (a_o), bulk modulus (B_0) values and formation energy (ΔH_f) of spinels $BaLu_2X_4$ (X = S, Se).

Spinels	a_o (Å)	B_o (GPa)	ΔH_f (eV/atom)
$BaLu_2S_4$	11.72	54.64	–1.01
$BaLu_2Se_4$	12.25	48.09	–0.92

In order to evaluate the studied spinels as thermodynamically stable, we calculate the formation (ΔH_f) energy by using the following expression:

$$\Delta H_f^{BaLu_2S_4} = E_t^{BaLu_2S_4} - E_t^{Ba\text{-cubic}} - 2E_t^{Lu\text{-hcp}} - 4E_t^{S\text{-Orthorhombic}} \quad (1)$$

$$\Delta H_f^{BaLu_2Se_4} = E_t^{BaLu_2Se_4} - E_t^{Ba\text{-cubic}} - 2E_t^{Lu\text{-hcp}} - 4E_t^{Se\text{-Trigonal}} \quad (2)$$

Here in above equations, total energies of studied spinels are represented as $E_t^{BaLu_2S_4}$ and $E_t^{BaLuSe_4}$ and individual Ba, Lu, S and Se stable elements total energy are represented as $E_t^{Ba\text{-cubic}}$, $E_t^{Lu\text{-hcp}}$, $E_t^{S\text{-Orthorhombic}}$ and $E_t^{Se\text{-Trigonal}}$, respectively. The calculated value of ΔH_f is tabulated in Table 1, which is –1.01 and –0.92 eV/atom for $BaLu_2S_4$ and $BaLu_2Se_4$, respectively. Both studied spinels showed a negative value for the ΔH_f, indicating a heat evolving reaction during the formation of the spinel and that it is an exothermic reaction. The evolution of heat makes compounds to hold less energy than their constituents which demonstrates their thermodynamic stability.

3.1.2 Opto-Electronic Properties

To accurately determine the electrical characteristics, it is imperative to have precise knowledge of the compound's band gaps. We fulfilled this criterion by utilizing a superior DFT exchanging potential to compute the frequency band configurations of $BaLu_2X_4$ (X = S, Se). The

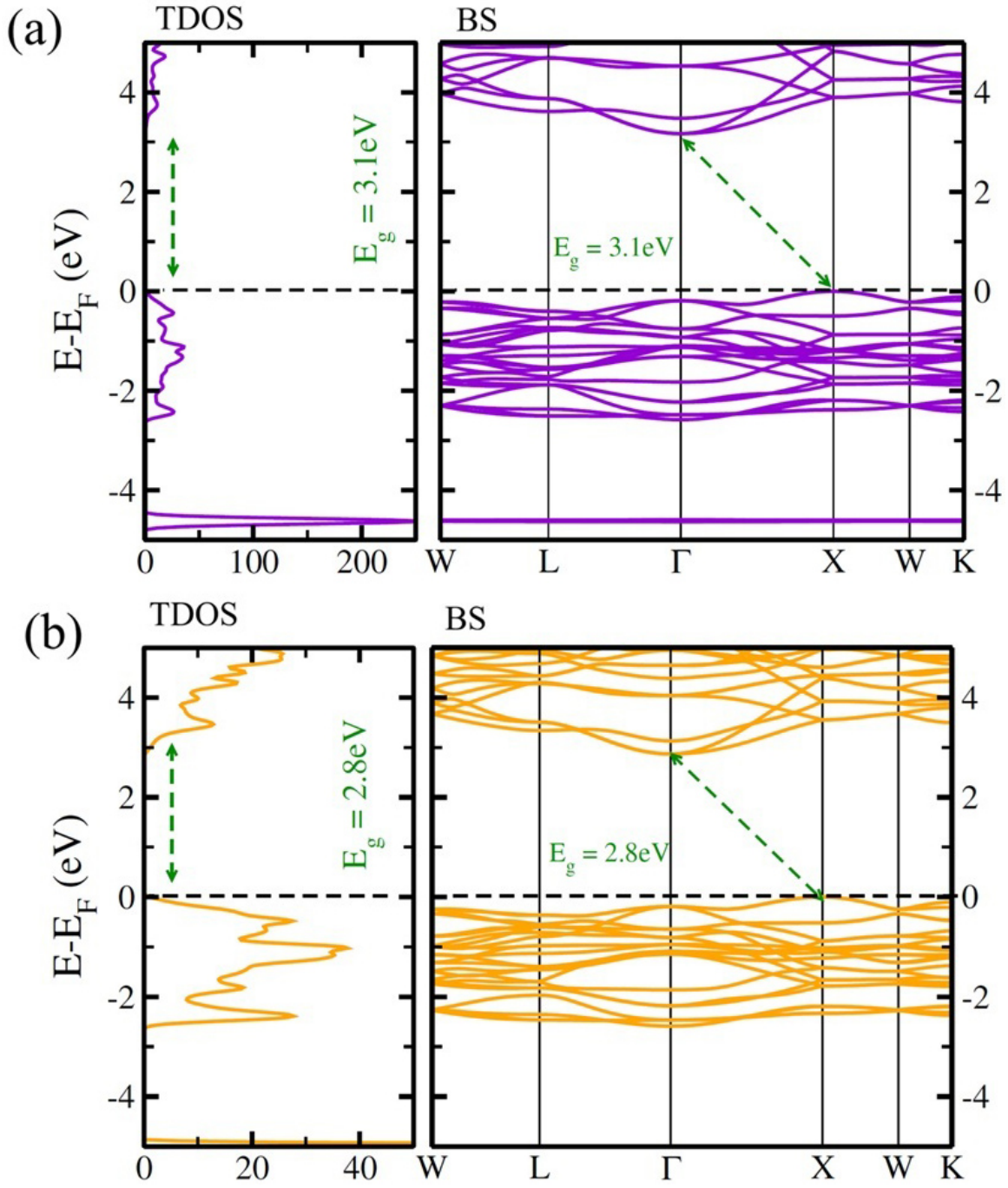

Fig. 2. Electronic band structure (BS) along total density of states (TDOS) of chalcogenide spinels (a) $BaLu_2S_4$ and (b) $BaLu_2Se_4$.

electronic band dispersion calculations for $BaLu_2X_4$ (X = S, Se) demonstrate that both materials possess a indirect band gap located at the Γ-X high-symmetry point. The computed band gap energies are approximately 3.1 eV for $BaLu_2S_4$ and 2.8 eV for $BaLu_2Se_4$, reflecting a clear narrowing of the gap when sulfur is substituted by selenium (see Fig. 2). This trend can be attributed to the comparatively larger ionic size and reduced electronegativity of selenium, which promote stronger orbital interactions and consequently reduce the energy separation between the valence and conduction bands. The indirect-gap nature of these compounds highlights their strong potential for applications in optoelectronic and photonic devices.

Further understanding of the electronic behavior is obtained through an analysis of the total density of states (TDOS) alongside the band structures, as shown in Fig. 2a,b. In both spinel systems, the upper valence band region is dominated by the p-states of the chalcogen atoms (S/Se), while the conduction band is primarily characterized by Lu-derived p-orbitals. Additional features arise from the hybridization between Lu-p and chalcogen-p states, whereas the contribution from Ba s-states remains minimal. This

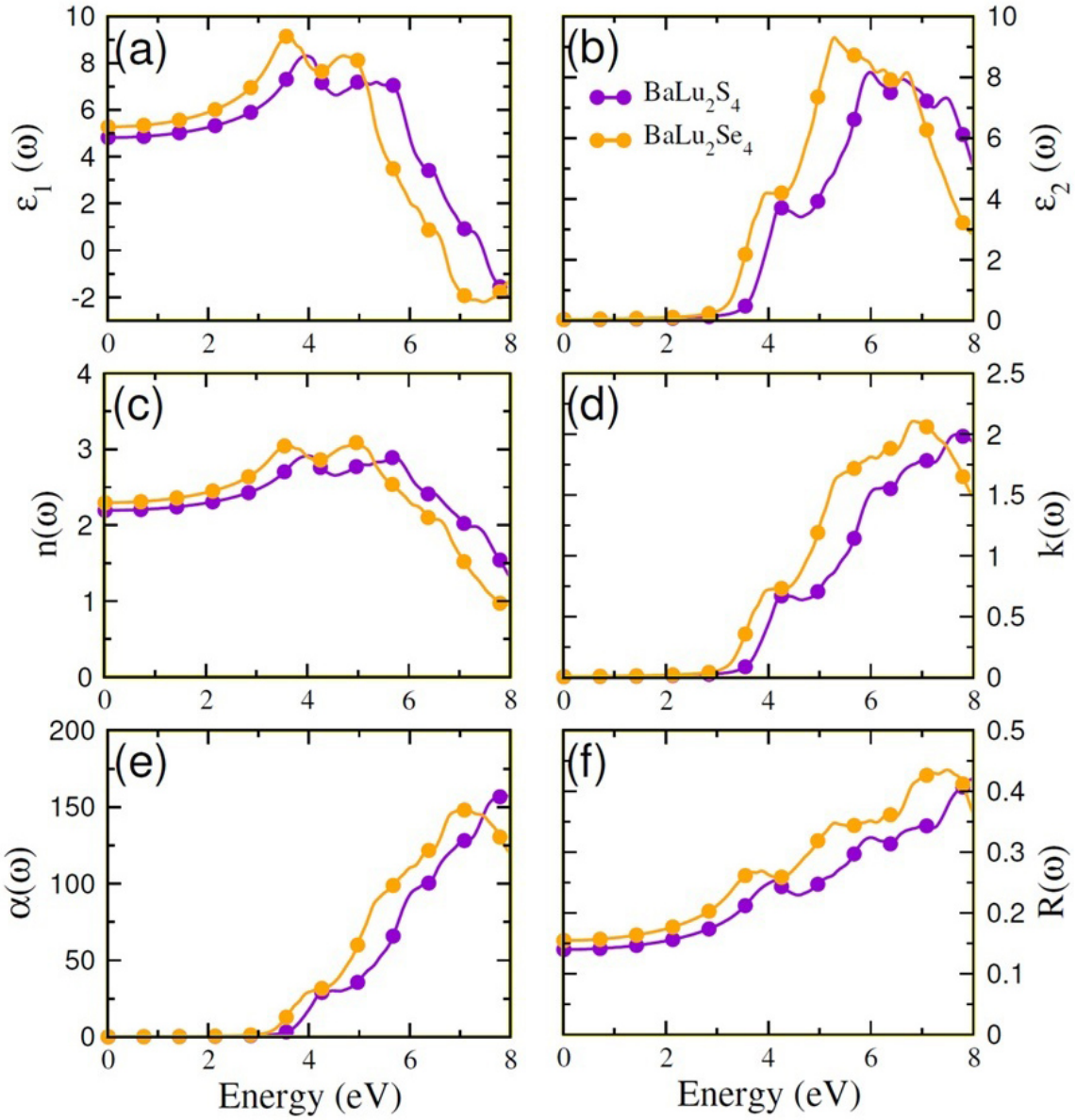

Fig. 3. The calculated (a) real part $\varepsilon_1(\omega)$, (b) imaginary part $\varepsilon_2(\omega)$, (c) refractive index $n(\omega)$, (d) the extinction coefficient $k(\omega)$, (e) absorption $\alpha(\omega)$ (10^4 cm^{-1}), (f) reflectivity $R(\omega)$ for $BaLu_2S_4$ and $BaLu_2Se_4$.

pronounced p–p orbital coupling between lutetium and sulfur/selenium atoms confirms the partially covalent bonding character and plays a critical role in establishing the indirect band gap along the Γ–X transition. The combined interpretation of the band structures and density of states underscores the suitability of $BaLu_2S_4$ and $BaLu_2Se_4$ for tailored electronic and optical device applications.

For material to be effective in optical applications, it must possess a direct band gap accompanied by efficient interband optical transitions [21]. Accordingly, all optical response functions were computed using a Lorentzian broadening factor of 0.1 eV. Since the TB-mBJ approach produced band gap values in good agreement with expected semiconductor behavior, only a negligible scissors correction was required. The real and imaginary parts of the dielectric function, together with refractive indices for $BaLu_2X_4$ (X = S, Se), are discussed in Fig. 3a,b. The real part of the dielectric function, $\varepsilon_1(\omega)$, governs light polarization and dispersion within the crystal, whereas the imaginary part, $\varepsilon_2(\omega)$, is directly related to optical absorption. Higher $\varepsilon_2(\omega)$ values indicate stronger photon absorption, while lower values correspond to increased transparency, further supporting the optical relevance of these chalcogenide spinels.

The frequency-dependent real part of the dielectric function, $\varepsilon_1(\omega)$, provides essential insight into the polarization behavior of $BaLu_2S_4$ and $BaLu_2Se_4$ under incident electromagnetic radiation. As presented in Fig. 3a, the real component of the dielectric function, $\varepsilon_1(\omega)$, exhibits pronounced resonance features at around 7.5 eV for $BaLu_2S_4$

and nearly 9.0 eV for $BaLu_2Se_4$, corresponding to the maximum polarization response of the crystal lattice under an external electromagnetic field. Beyond these resonance energies, particularly in the photon energy range of 3.5–4.0 eV, $\varepsilon_1(\omega)$ shows a sharp dispersion and becomes negative values mainly occurring around 7–8 eV, signifying a reduction in dielectric polarization. Such behavior is typically associated with plasma-like characteristics, wherein collective oscillations of charge carriers dominate, imparting transient metallic-like optical behavior to the material.

Further, static value of dielectric constant ($\varepsilon_1(0)$) is consistent with Penn's model [22], which relates the static dielectric constant $\varepsilon_1(0)$ inversely to the electronic band gap (E_g). The introduction of selenium leads to a narrower band gap and an expanded lattice parameter, both of which contribute to an increase in dielectric strength. This enhancement arises from the higher electronic polarizability and reduced effective nuclear binding in selenium-based compounds, enabling stronger lattice polarization under optical excitation. The imaginary part of the dielectric function, $\varepsilon_2(\omega)$, which directly reflects the optical absorption behavior, is obtained from $\varepsilon_1(\omega)$ via the Kramers–Kronig relations [23]. As illustrated in Fig. 3b, $\varepsilon_2(\omega)$ remains nearly zero at lower photon energies and increases rapidly once the incident photon energy surpasses the optical band gap. The absorption edges are located at approximately 3.1 eV for $BaLu_2S_4$ and 2.8 eV for $BaLu_2Se_4$, corresponding to the onset of interband electronic transitions. These thresholds align well with the direct band gap values derived from electronic band structure calculations, thereby validating the consistency of the optical analysis.

The variation of the refractive index $n(\omega)$, depicted in Fig. 3c, shows a smooth increase at lower photon energies as a result of enhanced electronic polarization, reaching a maximum in the vicinity of the resonance region. Subsequently, $n(\omega)$ decreases at higher photon energies as absorption becomes dominant. The extinction coefficient $k(\omega)$, presented in Fig. 3d, follows a similar trend to $\varepsilon_2(\omega)$, reinforcing the conclusion that strong absorption arises from interband transitions initiated beyond the band gap threshold.

The refraction and degradation in light intensity might be approximated based on the refractive index as well as the degree of extinction coefficients. The refractive index, $n(\omega)$ with the coefficient of extinction $k(\omega)$ have an association to refraction, as seen in Fig. 3c. The subsequent expressions elucidate the correlation between $n(\omega)$ & $k(\omega)$ along with $\varepsilon_1(\omega)$ and $\varepsilon_2(\omega)$ [24]:

$$n^2 - k^2 = \varepsilon_1(\omega) \tag{3}$$

$$2nk(\omega) = \varepsilon_2(\omega) \tag{4}$$

The $n(\omega)$ along with the real component of the coefficient of dielectric exhibit an analogous response, thus a maximum amount of $n(\omega)$ allows photon to pass across the material at the frequency at which the resonance occurs. The relationship between group velocity and phase velocity is given by this equation [25]:

$$V_g(1 - {}^{\lambda dn}/_{nd\lambda}) = \vartheta_P \tag{5}$$

Here, V_g represents the group velocity, ϑ_p represents the phase velocity, and λ represents the wavelength. Observation of integer levels of $n(\omega)$ occurs in the extremely energetic portion where the group velocity exceeds its phase velocity. Whenever both the susceptibility & permeability for a medium exhibit negative characteristics in the superluminal valley-shaped that substance undergoes a transition from being a right-hand towards a left-hand. In a similar vein the function $k(\omega)$ is correlated with the value of $\varepsilon_2(\omega)$ as depicted in the aforementioned equation and illustrated in Fig. 3b. When there is a correlation between absorption and extinction coefficients, it indicates that light will be absorbed.

$$\frac{\alpha}{k} = \frac{4\pi}{\lambda} \tag{6}$$

As shown in Fig. 3e, the value of the absorption coefficient $\alpha(\omega)$ remains very low for incident photons with energies below the fundamental band gap energy, signifying a high degree of optical transparency in the visible spectrum. However, as the spectrum shifts towards the near ultraviolet region, the value of $\alpha(\omega)$ increases sharply. Such a high degree of absorbance signifies high optical excitation efficiency in the material. Hence, this behavior clearly signifies the high photoactive nature of both $BaLu_2S_4$ and $BaLu_2Se_4$. The reflectivity spectrum $R(\omega)$ in Fig. 3f indicates medium reflectance in the visible energy range, with maximum reflectance in the photon energy range of 7.0 to 8.0 eV. Additionally, there is a non-zero reflectance at zero photon energy, which can be related to natural lattice vibrations in the crystal. The fact that these materials are of low reflectance in the visible range and high in absorption at higher photon energies further confirms their applicability in optical coatings and semiconductor-based photonic components. Overall, from the optical response analysis, it is seen that $BaLu_2S_4$ and $BaLu_2Se_4$ exhibit high near-ultraviolet absorption along with high transparency in the visible region. Here, high transparency in a particular region refers to low absorption.

3.1.3 Elastic Properties

Elastic constants serve as key indicators of the mechanical stability and elastic response of crystalline solids under external stress [26]. In the case of cubic spinel systems, mechanical behavior is completely described by a

Table 2. Calculated elastic constant (C_{11}, C_{12}, C_{44}) and their calculated bulk modulus (B), shear modulus (G), Young's modulus (Y), Poisson's ratio (ν) and Pugh ratio (B_0/G) for spinels $BaLu_2S_4$ and $BaLu_2Se_4$.

	C_{11} (GPa)	C_{12} (GPa)	C_{44} (GPa)	B_0 (GPa)	G (GPa)	Y (GPa)	ν	B_0/G
$BaLu_2S_4$	120.05	22.66	32.88	55.12	38.49	93.68	0.218	1.43
$BaLu_2Se_4$	108.81	18.55	26.91	48.63	33.14	81.09	0.221	1.46

limited set of independent elastic constants, (C_{11}, C_{12}, C_{44}) are sufficient to describe their mechanical response under applied stress. As listed in Table 2, both $BaLu_2S_4$ and $BaLu_2Se_4$ exhibit positive values of all elastic constants and satisfy the Born stability criteria for cubic ($C_{11} - C_{12} > 0$, $C_{12} < B_0 < C_{11}$, $C_{44} > 0$, and $C_{11} + 2C_{12} > 0$) confirming their mechanical stability. The longitudinal elastic constant C_{11}, which characterizes resistance to uniaxial compression, is higher for $BaLu_2S_4$ (120.05 GPa) than for $BaLu_2Se_4$ (108.81 GPa), indicating comparatively stronger directional bonding in the sulfide compound. Likewise, the shear-related constant C_{44} is larger for $BaLu_2S_4$ (32.88 GPa) than for $BaLu_2Se_4$ (26.91 GPa), which indicates that $BaLu_2S_4$ resists shear deformation more. Comparatively low values of C_{12} in both materials suggest that there are moderate interatomic interactions under transverse strain.

The elastic moduli at the macroscopic level provide further explanation of the mechanical properties of the spinels. The bulk modulus (B_0), which is related to resistance to volume compression, is larger in the case of $BaLu_2S_4$ (55.12) than in the case of $BaLu_2Se_4$ (48.63), which indicates higher incompressibility of the sulfide component. Also, the corresponding shear modulus (G) (38.49) and Young's modulus (Y) (93.68) of $BaLu_2S_4$ are larger, which indicates higher rigidity and stiffness, respectively, than in the case of $BaLu_2Se_4$, which has relatively low values of (G) (33.14) and (Y) (81.09) GPa.

Poisson's ratio (ν) is useful in understanding the nature of bonding and plasticity. The obtained (ν) values of near 0.22 in both compounds are indicative of materials with a bonding nature that is dominated by both ionic and covalent bonding and has moderate plasticity [27]. Moreover, the Pugh ratio (B_0/G) is a criteria function separating the brittle and ductile nature of the materials with the critical value of 1.75. The calculated (B_0/G) values of 1.43 and 1.46 for the $BaLu_2S_4$ and $BaLu_2Se_4$ compounds imply that the materials lie in the brittle side with a slightly higher tendency of ductility in the $BaLu_2Se_4$ compound. Overall, the elastic properties calculation, it has been verified once again that $BaLu_2S_4$ and $BaLu_2Se_4$ are stable in a cubic spinel structure as moderately rigid materials. The higher values for $BaLu_2S_4$ indicate that it is less susceptible to mechanical deformation, whereas $BaLu_2Se_4$ provides a small enhancement in ductility.

3.2 Photocatalytic and Thermodynamic Properties

3.2.1 Photocatalytic Properties

The photocatalytic efficiency of semiconducting materials is intrinsically linked to their electronic band structure, particularly the relative positions of the conduction band minimum (CBM) and VBM with respect to the redox potentials of the target reactions [28]. An effective photocatalyst for water splitting must simultaneously possess an appropriate band gap for broad solar absorption and a favorable band-edge alignment to drive both hydrogen evolution reaction (HER) and oxygen evolution reaction (OER). Specifically, the CBM should lie at a more negative potential than the H^+/H_2 redox level, while the VBM should be more positive than the H_2O/O_2 oxidation potential. In addition to band alignment, efficient charge-carrier separation, adequate thermodynamic driving force, and structural stability are critical factors influencing overall photocatalytic performance [29]. Consequently, theoretical assessment of band alignment provides a reliable criterion for evaluating the intrinsic photocatalytic potential of novel materials for solar energy applications.

The calculated band alignments of $BaLu_2S_4$ and $BaLu_2Se_4$ with respect to standard water-splitting redox potentials are presented in Fig. 4. $BaLu_2S_4$ exhibits a band gap of approximately 3.1 eV, with the CBM positioned at –1.98 eV and the VBM at –5.08 eV. The CBM lies well above the hydrogen reduction potential (0.0 V vs. NHE (normal hydrogen electrode)), indicating sufficient thermodynamic feasibility for proton reduction, while the VBM is located above the oxygen evolution potential (1.23 V vs. NHE), enabling effective water oxidation. This energetic configuration confirms that $BaLu_2S_4$ meets the essential requirements for overall photocatalytic water splitting [30].

In comparison, $BaLu_2Se_4$ possesses a narrower band gap of 2.8 eV, which improves its absorption in the visible region. The CBM of $BaLu_2Se_4$ is located at –2.78 eV, significantly more negative than the H^+/H_2 potential, providing an enhanced driving force for hydrogen evolution. Simultaneously, the VBM at –5.58 eV remains sufficiently positive relative to the oxygen evolution potential, ensuring effective water oxidation. Calculated CBM of $BaLu_2S_4$ (–1.98 eV) is positioned higher in the electron energy than that of $BaLu_2Se_4$ (–2.78 eV), consequently generating a higher thermodynamic driving force as compared to the reduction potential of the H^+/H_2 couple (–4.44 eV). Thus, the reduction ability of hydrogen evolution reaction (HER) is stronger in the case of $BaLu_2S_4$. The larger separation between the band edges and redox potentials in $BaLu_2Se_4$ suggests superior charge-transfer kinetics and reduced electron-hole recombination during photocatalysis [31]. A comparative evaluation indicates that while both $BaLu_2S_4$ and $BaLu_2Se_4$ satisfy the basic criteria

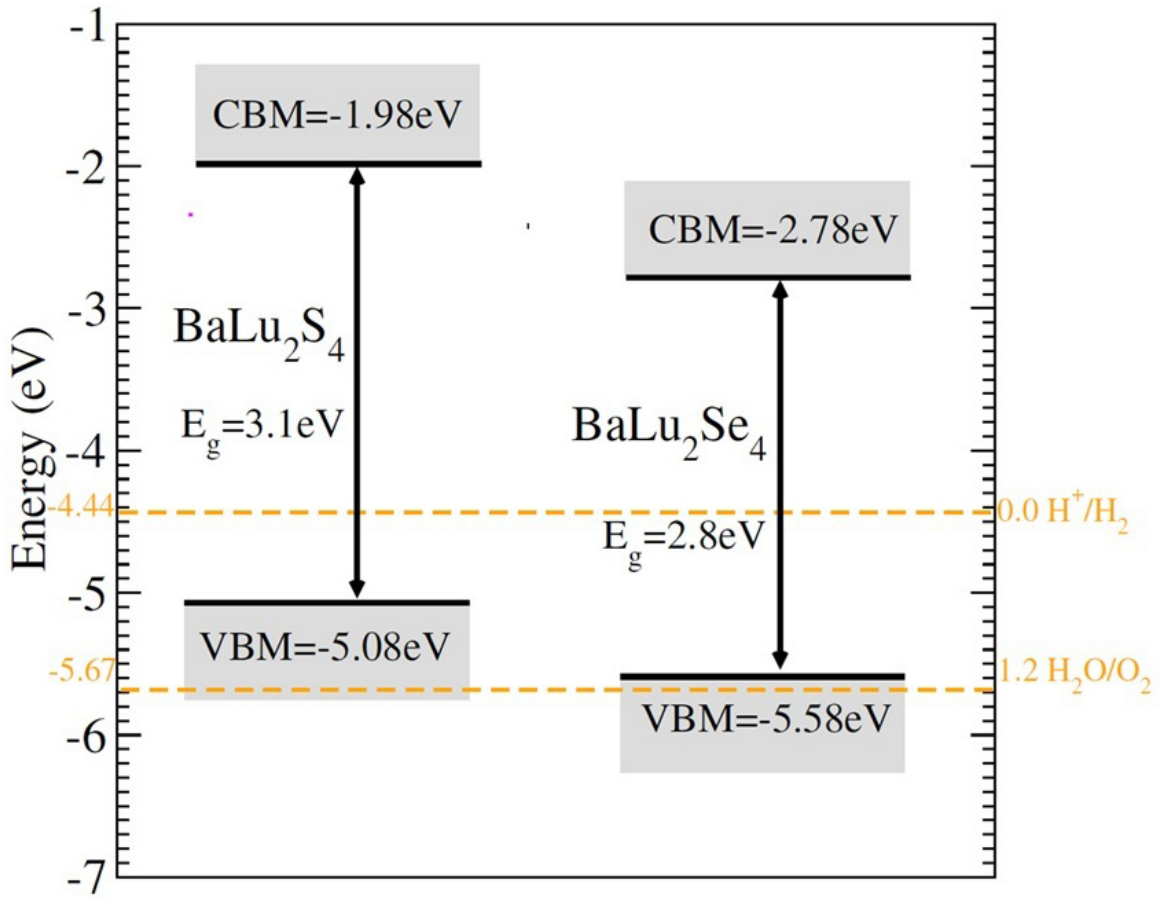

Fig. 4. The band-edge positions of $BaLu_2S_4$ and $BaLu_2Se_4$ displaying photocatalytic viability for water splitting.

for photocatalytic water splitting, $BaLu_2Se_4$ demonstrates superior potential for solar energy applications. Its narrower band gap allows for enhanced utilization of the solar spectrum, and the deeper CBM provides stronger reducing power for hydrogen generation. Furthermore, the favorable VBM alignment supports efficient oxygen evolution without compromising material stability. These characteristics collectively suggest that $BaLu_2Se_4$ is the more favorable candidate for visible-light-driven photocatalytic hydrogen production based on its more negative CBM and stronger reduction potential.

3.2.2 Thermodynamic Properties

Basic thermodynamic properties are of great importance in interpreting the thermal stability, lattice dynamics, and temperature-dependent behavior of crystalline solids. Thermodynamic parameters-the bulk modulus, Grüneisen parameter, heat capacities, entropy, Debye temperature, and the thermal expansion coefficient-offer profound insight into anharmonic lattice vibrations and phonon-mediated interactions. These parameters are vital for understanding the various high-temperature energy applications. In particular, the performed thermodynamic analysis is of primary importance for chalcogenide-based spinels like $BaLu_2S_4$ and $BaLu_2Se_4$ due to the strong interdependence between structural rigidity and vibrational characteristics. Fig. 5 illustrates the calculated temperature-dependent thermodynamic properties for a wide temperature range with the aim of comparative assessment of the lattice stability and thermal response of the $BaLu_2S_4$ and $BaLu_2Se_4$ phases.

Temperature-dependent thermodynamic properties for $BaLu_2S_4$ and $BaLu_2Se_4$ have been investigated by first-principles calculations based on density functional theory, within the full-potential linearized augmented plane wave approach as implemented in the WIEN2k package. The ground-state structural parameters have been calculated with the total-energy minimization method concerning unit-cell volume. Then, the obtained energy–volume relation has been fitted within an appropriate equation-of-state model to extract mechanical parameters such as bulk modulus and its first-order pressure derivative. Thermodynamic functions, namely, heat capacity, entropy, Debye temperature, thermal expansion coefficient, Grüneisen parameter, and Gibbs free energy, have been calculated in a wide temperature range by using the so-called quasi-harmonic Debye model. It takes into account the vibrational contributions through the volume dependence of the lattice dynamics. This theoretical approach assures an accurate description of the anharmonic thermal response

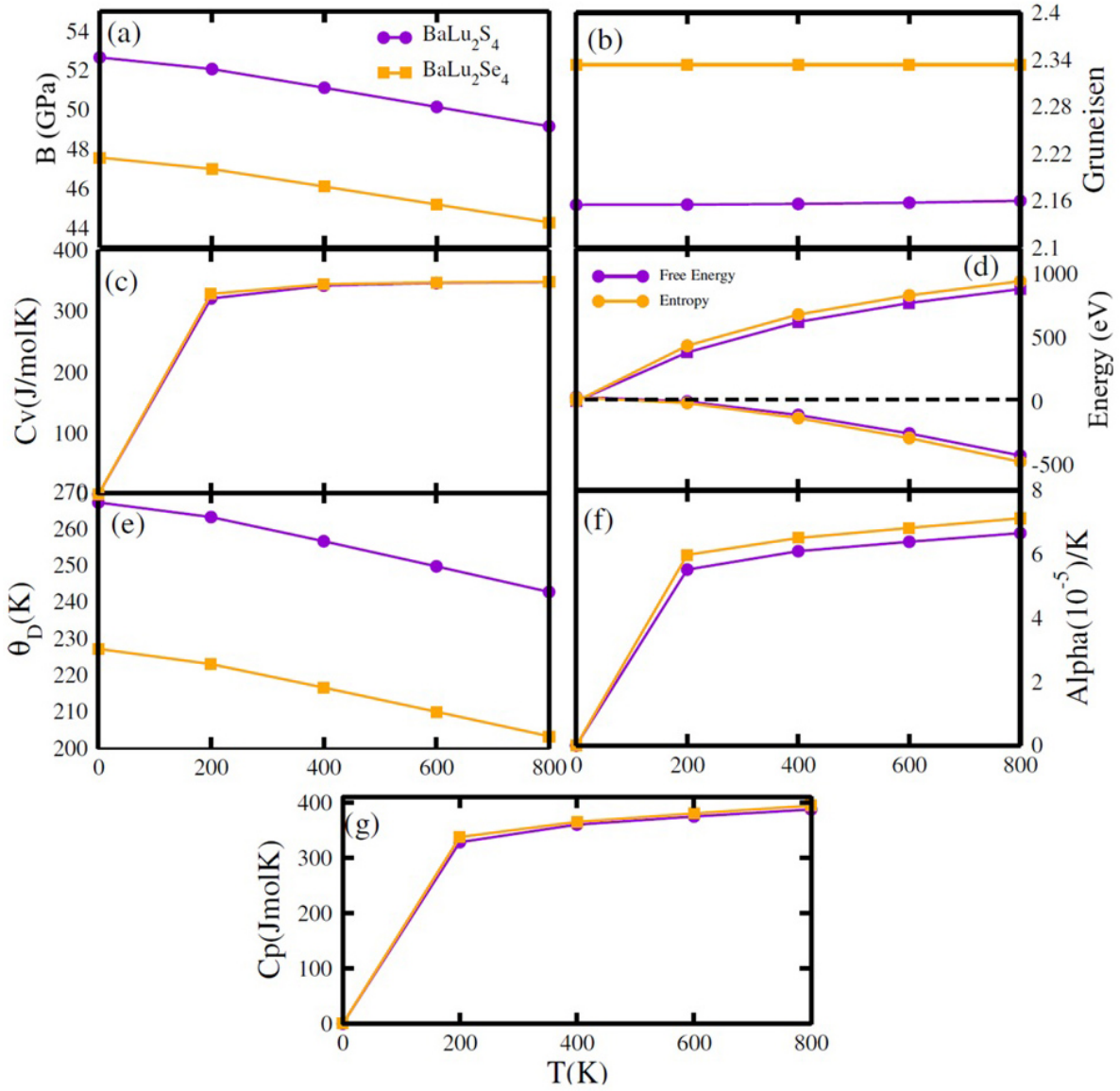

Fig. 5. Calculated thermodynamic properties of $BaLu_2S_4$ and $BaLu_2Se_4$ (a) bulk modulus (GPa) (b) Grüneisen (c) heat capacity at constant volume (C_v), (d) free energy and entropy (S), (e) Debye temperature, (f) thermal expansion (α) and (g) heat capacity of at constant pressure (C_p).

and constitutes a reliable tool for predicting the lattice stability and thermal behavior of the studied compounds along an extended temperature range.

Fig. 5a depicts the temperature dependence of the bulk modulus (Bs) for $BaLu_2S_4$ and $BaLu_2Se_4$. For both compounds, the bulk modulus decreases monotonically with increasing temperature, a typical behavior for crystalline solids. This deterioration results from thermal expansion and increased anharmonicity of lattice vibrations, leading to a gradual weakening of interatomic bonds at higher temperatures. In particular, $BaLu_2S_4$ exhibits higher values of bulk modulus compared with $BaLu_2Se_4$ throughout the temperature range, which means that its lattice is harder and more resistant to volume deformation. $BaLu_2Se_4$ exhibits lower bulk modulus due to the larger ionic radius and higher mass of selenium compared to sulfur, resulting in softer lattice interactions. The Grüneisen parameter plotted in Fig. 5b shows the state of anharmonicity in lattice vibrations. The Grüneisen parameter is almost temperature-independent for both $BaLu_2S_4$ and $BaLu_2Se_4$, which suggests that anharmonic effects do not change much over the studied temperature range. $BaLu_2Se_4$ has a larger Grüneisen value than $BaLu_2S_4$, which implies greater strength of phonon–phonon interactions and thus stronger anharmonicity within this selenium compound. This is consistent with the softer bonding and the greater lattice flexibility with heavier chalcogen atoms.

Fig. 5c shows the temperature dependence of constant-volume heat capacity, C_v. At low temperature, C_v rises steeply for both compounds owing to the succes-

sive excitation of the low-frequency phonon modes, and at further higher temperature, C_v tends to saturate at a value close to the classical Dulong–Petit limit, reflecting the complete excitation of the vibrational degree of freedom. $BaLu_2Se_4$ displays a slightly higher C_v value compared with $BaLu_2S_4$, which may be attributed to its lower phonon frequencies and the increased vibrational contribution from the heavier atomic mass. Fig. 5d illustrates the variation of free energy and entropy versus temperature for $BaLu_2S_4$ and $BaLu_2Se_4$. The Gibbs free energy is found to decrease monotonically with increasing temperature for both materials, indicating that entropic contributions become more dominating at high temperatures. Such a trend constitutes evidence for the thermodynamic stability of both compounds up to all the explored temperatures [32,33]. Entropy increases linearly with temperature, reflecting the increase in accessible phonon states. As can be observed, $BaLu_2Se_4$ exhibits marginally higher entropy values compared to $BaLu_2S_4$, indicating higher lattice disorder and greater vibrational freedom, consistent with its lower calculated stiffness and stronger anharmonic character. Fig. 5e illustrates the variation of the Debye temperature (θ^D) as a function of temperature for the title spinel systems. For $BaLu_2S_4$ and $BaLu_2Se_4$, θ^D decreases gradually with temperature rise, indicating lattice softening due to thermal vibrations [34]. $BaLu_2S_4$ exhibits a higher Debye temperature within the investigated temperature range, pointing towards higher average phonon frequencies and stronger interatomic bonding. On the other hand, the smaller θ^D values in $BaLu_2Se_4$ reflect softer lattices with lower vibrational stiffness, thus supporting its higher degree of anharmonicity.

Fig. 5f shows the thermal expansion coefficient (α) versus temperature. At low temperatures, α increases sharply and then rises more gradually at higher temperatures; this arises from increased anharmonic lattice vibrations with increasing thermal energy [35]. $BaLu_2Se_4$ exhibits a larger α than $BaLu_2S_4$, which is consistent with its smaller bulk modulus and larger Grüneisen parameter. This indicates that $BaLu_2Se_4$ is more sensitive to volumetric expansion upon thermal excitation.

Fig. 5g depicts C_p versus temperature. Similar to the variation in C_v, C_p also rises steeply at low temperatures and increases gradually toward a saturation value at elevated temperatures [36]. The deviation of C_p from C_v is more noticeable at higher temperatures because of the additional contribution from thermal expansion. C_p for $BaLu_2Se_4$ is relatively higher than that of $BaLu_2S_4$ at all temperatures, indicating increased anharmonicity and thereby higher thermal expansion.

3.3 Limitations of the Study

This work is based on density functional theory calculations, and like all theoretical studies, the results depend on the approximations used within the computational framework. Although the TB-mBJ approach provides improved band gap estimation compared to standard GGA methods, it does not fully account for many-body interactions or excitonic effects that may influence the electronic structure. The thermodynamic properties were analyzed using the quasi-harmonic Debye model, which assumes moderate anharmonicity and may not completely describe lattice behavior at very high temperatures. In addition, the photocatalytic assessment relies on bulk band-edge alignment and does not include the possible influence of surface states, intrinsic defects, carrier recombination processes, or material synthesis conditions, all of which can affect experimental performance. Therefore, further experimental investigation and the use of more advanced computational techniques would be valuable to validate and extend the present findings.

4. Conclusion

DFT is used in this study to carry out an analytical investigation into the properties of Lu-based spinels $BaLu_2X_4$ (X = S, Se). The main point is that first-principles calculations have confirmed that $BaLu_2S_4$ and $BaLu_2Se_4$ are stable semiconducting spinels that possess tunable electronic, optical, and thermal properties controlled by chalcogen substitution. Replacing S by Se expands the lattice, reducing the indirect band gap from 3.1 eV to 2.8 eV, leading to the extension of optical response toward the visible range and enhanced light-matter interaction. Optical analysis indicates strong dielectric polarization, significant absorption in the visible to near-ultraviolet range, and moderate reflectivity, showing potential for applications in optoelectronics and photonics. Thermodynamic and transport studies further suggest that $BaLu_2S_4$ exhibits higher mechanical rigidity and thermal robustness, while $BaLu_2Se_4$ shows stronger anharmonic behavior and better solar energy utilization. Favorable band edge alignment with the water redox potentials points to the intrinsic photocatalytic capability of both compounds, while $BaLu_2Se_4$ is the more favorable candidate for visible-light-driven photocatalytic hydrogen production based on its more negative CBM and stronger reduction potential.

Availability of Data and Materials

The corresponding author will provide the data generated during the study upon a reasonable request.

Author Contributions

The article was the result of the collective efforts of the complete team of authors. The written work was conceptualized by SMa and HOE, who also guided the entire project. The DFT computations were conducted by HHR, MUK, and MAJ, and they also collaborated on the entire manuscript. This manuscript's analysis of figures and tables were prepared by SMu. All authors contributed to ed-

itorial changes in the manuscript. All authors read and approved the final manuscript. All authors have participated sufficiently in the work and agreed to be accountable for all aspects of the work.

Ethics Approval and Consent to Participate

Not applicable.

Acknowledgment

Not applicable.

Funding

This research was funded by Ongoing Research Funding program - Research Chairs (ORF-RC-2026-5506), King Saud University, Riyadh, Saudi Arabia.

Conflicts of Interest

The authors declare no conflicts of interest.

References

[1] Wang Q, Domen K. Particulate Photocatalysts for Light-Driven Water Splitting: Mechanisms, Challenges, and Design Strategies. Chemical Reviews. 2020; 120: 919–985. https://doi.org/10.1021/acs.chemrev.9b00201

[2] Hisatomi T, Kubota J, Domen K. Recent advances in semiconductors for photocatalytic and photoelectrochemical water splitting. Chemical Society Reviews. 2014; 43: 7520–7535. https://doi.org/10.1039/c3cs60378d

[3] Ran J, Jaroniec M, Qiao SZ. Cocatalysts in Semiconductor-based Photocatalytic CO_2 Reduction: Achievements, Challenges, and Opportunities. Advanced Materials (Deerfield Beach, Fla.). 2018; 30: 1704649. https://doi.org/10.1002/adma.201704649

[4] Li X, Yu J, Low J, Fang Y, Xiao J, Chen X. Engineering heterogeneous semiconductors for solar water splitting. Journal of Materials Chemistry a. 2015; 3: 2485–2534. https://doi.org/10.1039/c4ta04461d

[5] Luo B, Song R, Geng J, Liu X, Jing D, Wang M, et al. Towards the prominent cocatalytic effect of ultra-small CoP particles anchored on g-C3N4 nanosheets for visible light driven photocatalytic H2 production. Applied Catalysis B: Environmental. 2019; 256: 117819. https://doi.org/10.1016/j.apcatb.2019.117819

[6] Chen X, Shen S, Guo L, Mao SS. Semiconductor-based photocatalytic hydrogen generation. Chemical Reviews. 2010; 110: 6503–6570. https://doi.org/10.1021/cr1001645

[7] Noor NA, Nasrullah F, Moussa IM, Mumtaz S. Mechanical, magnetic, and electronic characteristics of Sm-based chalcogenides for spintronics and device applications. Chalcogenide Letters. 2024; 21: 413–421. https://doi.org/10.15251/CL.2024.215.413

[8] Dixit A, Ahmed IA, Abraham JA, El-Bahy ZM, Manzoor M, Dar SA, et al. Optoelectronic and thermoelectric properties of spinel chalcogenides HgLa2X4 (X = S and Se): a first-principles study. Journal of Rare Earths. 2024; 42: 1927–1936. https://doi.org/10.1016/j.jre.2023.11.014

[9] Mahmood A, Ramay SM, Al-Masry W, Al-Zahrani AA, Al-Garadi NYA. Analyzing opto-electronic and transport characteristics of ZnSc2Se4 and CdSc2Se4 spinels for opto-electronic and energy storage devices. Modern Physics Letters B. 2021; 35: 2150184. https://doi.org/10.1142/S0217984921501840

[10] Althib H, Flemban TH, Aljameel AI, Mera A, Ashiq MGB, Mahmood Q, et al. First-principle study of electronic, optical and transport properties for (Zn/Cd)Sc2Se4 spinel chalcogenides. Bulletin of Materials Science. 2021; 44: 254. https://doi.org/10.1007/s12034-021-02544-w

[11] Xiong R, Sun Y, Li J, Chen K, Liu F, Xiao Y, et al. MgCr2O4/MgIn2S4 spinel/spinel S-scheme heterojunction: a robust catalyst for photothermal-assisted photocatalytic CO2 reduction. Inorganic Chemistry. 2024; 63: 19309–19321. https://doi.org/10.1021/acs.inorgchem.4c03044

[12] Yan D, Li K, Yan Y, Huang S, Von Lim Y, Shang Y, et al. Cubic spinel XIn2S4 (X= Fe, Co, Mn): a new type of anode material for superfast and ultrastable Na-ion storage. Advanced Energy Materials. 2021; 11: 2102137. https://doi.org/10.1002/aenm.202102137

[13] Qian GL, Xie Q, Liang Q, Luo XY, Wang YX. Electronic properties and photocatalytic water splitting with high solar-to-hydrogen efficiency in a hBNC/Janus WSSe heterojunction: first-principles calculations. Physical Review B. 2023; 107: 155306. https://doi.org/10.1103/PhysRevB.107.155306

[14] Chandrasekaran S, Bowen C, Zhang P, Li Z, Yuan Q, Ren X, et al. Spinel photocatalysts for environmental remediation, hydrogen generation, CO2 reduction and photoelectrochemical water splitting. Journal of Materials Chemistry A. 2018; 6: 11078-11104. https://doi.org/10.1039/C8TA03669A

[15] Zhang L, Ran J, Qiao SZ, Jaroniec M. Characterization of semiconductor photocatalysts. Chemical Society Reviews. 2019; 48: 5184-5206. https://doi.org/10.1039/C9CS00172G

[16] Tan HL, Abdi FF, Ng YH. Heterogeneous photocatalysts: an overview of classic and modern approaches for optical, electronic, and charge dynamics evaluation. Chemical Society Reviews. 2019; 48: 1255-1271. https://doi.org/10.1039/C8CS00882E

[17] Blaha P, Schwarz K, Madsen GKH, Kvasnicka D, Luitz J. WIEN2K: An Augmented Plane Wave + Local Orbitals Program for Calculating Crystal Properties. Technische Universität Wien: Vienna. 2001.

[18] Perdew JP, Ruzsinszky A, Csonka GI, Vydrov OA, Scuseria GE, Constantin LA, et al. Restoring the density-gradient expansion for exchange in solids and surfaces. Physical Review Letters. 2008; 100: 136406. https://doi.org/10.1103/PhysRevLett.100.136406

[19] Tran F, Blaha P. Accurate band gaps of semiconductors and insulators with a semilocal exchange-correlation potential. Physical Review Letters. 2009; 102: 226401. https://doi.org/10.1103/PhysRevLett.102.226401

[20] Al-Qaisi S, Rai D, Alshahrani T, Ahmed R, Haq BU, Tahir SA, et al. Structural, elastic, thermodynamic, electronic, optical and thermoelectric properties of MgLu2X4 (X= S, Se) spinel compounds from ab-initio calculations. Materials Science in Semiconductor Processing. 2021; 128: 105766. https://doi.org/10.1016/j.mssp.2021.105766

[21] Aguilera I, Palacios P, Sánchez K, Wahnón P. Theoretical optoelectronic analysis of MgIn2S4 and CdIn2S4 thiospinels: effect of transition-metal substitution in intermediate-band formation. Physical Review B—Condensed Matter and Materials Physics. 2010; 81: 075206. https://doi.org/10.1103/physrevb.81.075206

[22] Penn DR. Wave-Number-Dependent Dielectric Function of Semiconductors. Physical Review. 1962; 128: 2093–2097. https://doi.org/10.1103/physrev.128.2093

[23] Marius G. Kramers–Kronig Relations. The Physics of Semiconductors (pp. 775). Springer: Berlin Heidelberg. 2010.

[24] Wooten F. Optical Properties of Solids. Academic Press: New York. 1972.

[25] Noor N, Rashid M, Alay-e-Abbas S, Raza M, Mahmood A, Ramay SM, et al. Shift of indirect to direct bandgap and thermoelectric response of the cubic BiScO3 via DFT-mBJ studies. Ma-

terials Science in Semiconductor Processing. 2016; 49: 40–47. https://doi.org/10.1016/j.mssp.2016.03.014
[26] Mouhat F, Coudert FX. Necessary and sufficient elastic stability conditions in various crystal systems. Physical Review B. 2014; 90: 224104. https://doi.org/10.1103/PhysRevB.90.224104
[27] Wu DH, Wang HC, Wei LT, Pan RK, Tang BY. First-principles investigation of the structural stability and elastic characteristics of MgPd3 and its hydride. Journal of Magnesium and Alloys. 2014; 2:165–174. https://doi.org/10.1016/j.jma.2014.06.001
[28] Zhai M, Zhang Y, Xu J, Lin H, Xing J, Wang L. Correlation between existential form of ruthenium cocatalyst and photocatalytic hydrogen evolution of carbon nitride. Journal of Colloid and Interface Science. 2024; 673: 267–274. https://doi.org/10.1016/j.jcis.2024.06.092
[29] Opoku F, Govender KK, van Sittert CGCE, Govender PP. Recent progress in the development of semiconductor-based photocatalyst materials for applications in photocatalytic water splitting and degradation of pollutants. Advanced Sustainable Systems. 2017; 1: 1700006. https://doi.org/10.1002/adsu.201700006
[30] Fu SW, Yang J, Zhao ZY, Shan BF, Zhang JX, Zhang J, et al. Band-edge electronic structure on photo(electro)catalytic performance of ABO2 (A = Cu, Ag; B = Al, Ga, In): elucidating the role of valence electron states. Chemistry of Materials. 2024; 36: 3177–3190. https://doi.org/10.1021/acs.chemmater.3c02898
[31] Khan K, Rehman ZU, Yao S, Bajpai OP, Miotello A, Nawaz M, et al. Nanoscale engineering of semiconductor photocatalysts boosting charge separation for solar-driven H2 production: recent advances and future perspective. Nanotechnology Reviews. 2024; 13: 20240104. https://doi.org/10.1515/ntrev-2024-0104
[32] Blanco MA, Francisco E, Luaña V. GIBBS: isothermal-isobaric thermodynamics of solids from energy curves using a quasi-harmonic Debye model. Computer Physics Communications. 2004; 158: 57–72. https://doi.org/10.1016/j.comphy.2003.12.001
[33] Otero-de-la-Roza A, Luaña V. Gibbs2: a new version of the quasi-harmonic model code. I. Robust treatment of the static data. Computer Physics Communications. 2011; 182: 1708–1720. https://doi.org/10.1016/j.cpc.2011.04.016
[34] Anwar A, Noor NA, Mustafa GM, Atiq S, Ibrahim A, Laref A. Mechanically robust and thermodynamically stable $FeSc_2Z_4$ (Z = S, Se) spinels for future spintronic architectures. RSC Advances. 2025; 15: 35770–35781. https://doi.org/10.1039/d5ra04959h
[35] Steele JA. Atomistic origins of anharmonic lattice dynamics and thermal expansion in perovskite photovoltaics. Nature Energy. 2026; 11: 372–386. https://doi.org/10.1038/s41560-025-01938-y
[36] Gurunani B, Ghosh S, Gupta DC. Comprehensive investigation of half Heusler alloy: Unveiling structural, electronic, magnetic, mechanical, thermodynamic, and transport properties. Intermetallics. 2024; 170: 108311. https://doi.org/10.1016/j.intermet.2024.108311